In-Situ Micromechanical Testing in Scanning Electron Microscopy

R. Sarvesha and Sudhanshu S. Singh

1 Introduction

In-situ electron microscopy is a fast-growing and leading field in the materials research. It is an indispensable tool in understanding the material behavior in real-time. Additionally, the rapid miniaturization of the components for technological devices, that approaches micron and nanoscale dimensions, requires accurate size-specific properties (Gianolaet 2011) as it has been shown that the properties at a small length scale can be significantly different from the bulk counterpart (Dimiduk et al. 2005; Uchic et al. 2004; Volkert et al. 2008). Besides, in the multi-phase materials, the properties measured at a small length scale can be used as input to carry out microstructure-based modeling, which further assists in understanding the bulk deformation behavior (Guo et al. 2014).

To understand the material behavior in real-time, and at small length scales, a number of improvements in the microscopy techniques have been made over the years. Several two-dimensional (2D) microscopy techniques [e.g., optical, Raman, scanning electron microscopy (SEM), electron backscattered diffraction (EBSD), electron channeling contrast imaging (ECCI)] and three-dimensional (3D) techniques [e.g., transmission electron microscopy (TEM), X-ray tomography, neutron imagining, atom probe tomography (APT), focused ion beam (FIB) tomography] cover a range of length scales (Singh et al. 2014a,2015,2017; Gianolaet 2011; Volkert et al. 2008; Guo et al. 2014; Legros et al. 2010). Among these, the electron microscopy technique is well suited to elucidate the microstructural changes, with time, for micron- and submicron-sized specimens.

In-situ electron microscopy can be used to understand different phenomena depending upon the attachments equipped in SEM. For instance, a customized or commercial mechanical testing jig assists in unraveling the complex deformation mechanisms (Singh et al. 2014a). Further, EBSD and digital image correlation (DIC) techniques can assist in understanding the strain partitioning between different phases or grains in the materials. Novel microscopy techniques, such as electron channeling contrast imaging (ECCI) (Slama et al. 2019), can further assist in the quantification of the deformation systems generated under the application of load. FIB machining and deposition enable the sample preparation, which aids in evaluating the site-specific properties at small length scales using specialized attachments, such as nanoindentation system in a SEM (Sarvesha et al. 2020; Guo et al. 2014; Singh et al. 2014b). In recent years, irradiation properties of the nuclear materials have been studied by irradiating different ions, such as Fe+ , W+, He+, on the microscale test structures in assistance with FIB (Armstrong et al. 2015). Furthermore, a couple of *in-situ* SEM studies have also been carried out to evaluate the corrosion properties in environmental SEM (Proff et al. 2010), where a special *in-situ* jig was used to simulate the corrosion environment (Kim et al. 2020).

A powerful way of capturing real-time deformation microstructure is acoustic emission (AE) along with the conventional *in-situ* measurements. The AE method is based on sound emitted due to the activation of deformation mechanisms or fracture during deformation and thus provides highly time-resolved information (Wisner et al. 2015).

Figure 1 summarizes the various *in-situ* tests performed in SEM. *In-situ* tests in combination with SE/BSE imaging and EBSD in SEM are the most attractive methods used to understand the deformation behavior. This article discusses a few case studies showing the use of *in-situ* electron microscopy in evaluating the deformation behavior of metallic systems (Sn whisker, 7075 aluminum alloys, and AZ80 magnesium alloy).

R. Sarvesha · S. S. Singh (✉)
Department of Materials Science and Engineering, IIT Kanpur, Kanpur, India
e-mail: sudhanss@iitk.ac.in

2 Case Studies

2.1 Case Study I: *In-Situ* Tensile Behavior of Sn Whiskers

Environment-friendly Pb-free solders are predominantly based on Sn-rich alloys, where whiskers are known to grow on the Sn plates (Mathew et al. 2009). An understanding of the mechanical response of Sn whisker is vital for the soldering community. Whiskers are single crystals and contain minimal defects, which assists in the free flow of electron, thus making them an excellent conductor. The phenomenon of Sn whisker formation has been studied for decades (Galyon 2005); however, only a few studies have been performed to evaluate the mechanical properties of Sn whiskers (Dunn 1987; Powell and Skove 2004). This is due to adversity involved in handling whiskers. This case study deals with the *in-situ* evaluation of tensile properties of Sn whisker using a micro–electro–mechanical system (MEMS) tensile stage in assistance with a focused ion beam (FIB) (Singh et al. 2014a).

Sn whiskers on a Sn plate, having a very high aspect ratio, are shown in Fig. 2a. The steps of *in-situ* sample preparation using FIB are shown in Fig. 2. Manipulator needle was brought close to the base of the Sn whisker (Fig. 2b) and carefully welded using Pt (Fig. 2c). Sn whisker was then cut using Ga ions, as shown in Fig. 2d. The whisker was then brought to the MEMS device and welded in the trenches using Pt, as shown in Fig. 2e–g. In the end, the needle was released by cutting the whisker using Ga ions (Fig. 2h).

The MEMS device is shown in Fig. 3a (details of construction of the MEMS stage are reported elsewhere (Han and Saif 2006; Han et al. 2007)), and welded whisker on it is shown in Fig. 3b. A quasistatic loading was applied during the tensile test until fracture. The fractured Sn whisker is shown in Fig. 3c. The magnified image of the whisker shows that its surface is irregular. Therefore, to evaluate the stress, the surface area was calculated using image processing software (ImageJ), as shown in Fig. 3d. Two

successful tests were performed, and in both the case linear stress–strain behavior was observed for the Sn whisker (Fig. 3e). The values of Young's modulus of both the whiskers were measured to be 42 and 45 GPa, which are close to the theoretical value of the modulus for pure Sn. The fracture strength and strain to failure for the two tests were 720 MPa, 880 MPa, and 2%, 3%, respectively. The observed high fracture strength and limited ductility may be attributed to a lack of defects in the single crystal Sn whiskers.

Limited *ex-situ* experiments have been performed to evaluate the mechanical properties of Sn whiskers (Dunn 1987; Powell and Skove 2004). Powell and Skove (2004) observed the linear load–displacement behavior. However, the properties of the whiskers were not reported. Dunn (1987) obtained Young's modulus using the cantilever method. However, a large variability (8–85 GPa) was observed. One of the crucial shortcomings in Dunn's study was the measurement of the cross-sectional area in which the whisker was assumed to have a circular cross section. However, it should be noted that in the bending theory, Young's modulus varies with the fourth power of the radius, and thus, a small change in the radius would result in a significant deviation in the measurement of modulus. In comparison with the *ex-situ* testing, which had inherent limitations in handling the whiskers, the *in-situ* tensile testing in SEM assisted in evaluating the reliable mechanical properties of the Sn whisker.

2.2 Case Study II: Evaluation of Mechanical Properties of the Constituent Particles in Al 7075 by Micro-pillar Compression

Aluminum alloys are predominantly used as structural materials due to their high strength-to-weight ratio (Bucci et al. 2000; Starke and Staley 2011). These alloys contain second-phase particles (Fe-containing: Al_7Cu_2Fe and Si-containing: Mg_2Si), also called as constituent particles, which form during casting and do not dissolve in the
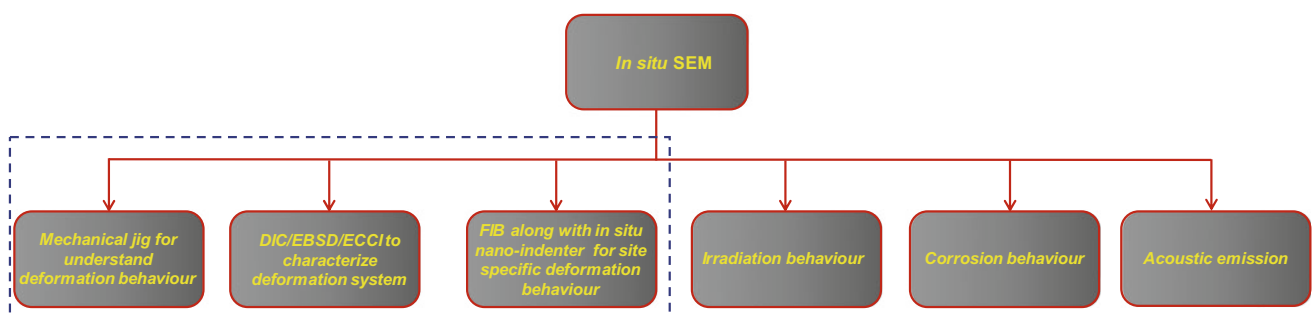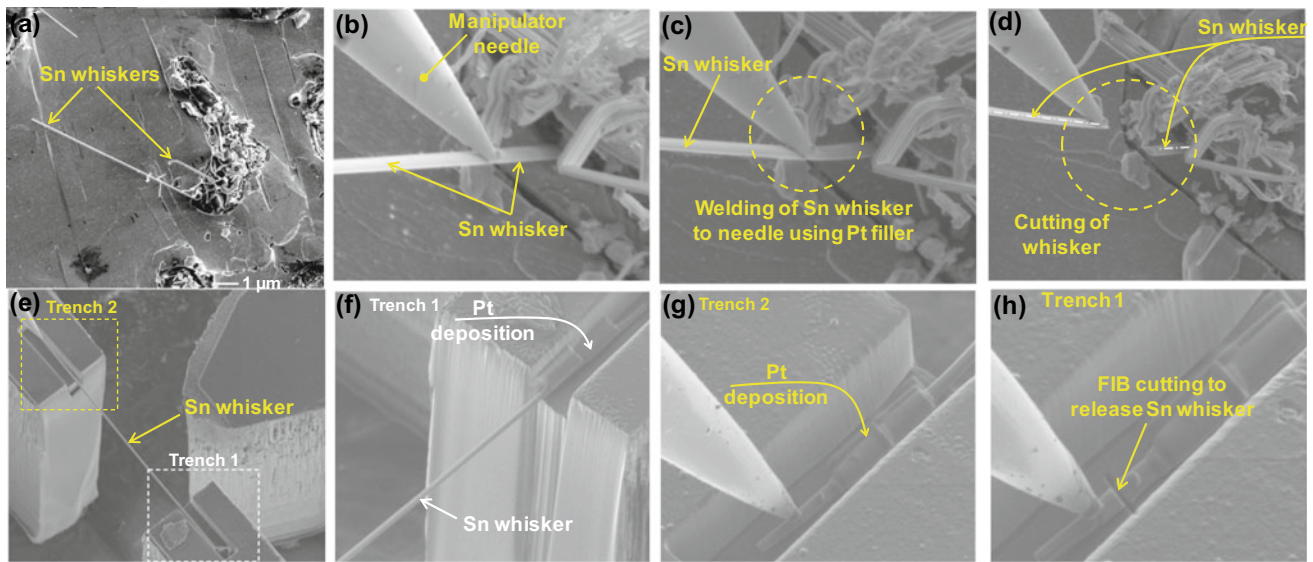

Fig. 1 Summary of the *in-situ* test performed in a scanning electron microscope

Fig. 2 a SEM image of Sn whiskers. Steps of whisker lift off and placement in MEMS inside FIB/SEM, **b** manipulator needle in contact with whisker, **c** welding of whisker using Pt filler, **d** FIB cutting of the whisker, **e–g** placement and welding of whisker in the trenches, and **h** FIB cutting to release the needle (Singh et al. 2014a)

subsequent thermomechanical treatment of the alloy (Payne et al. 2010; Xue et al. 2007). These particles have been observed to affect the overall deformation behavior of the alloy as they are the source for crack nucleation and propagation during static or dynamic loading (Pearson 1975; Weiland et al. 2009; Maire et al. 2011; Lugo et al. 2011). Hence, the overall mechanical response of the Al7075 alloy depends on the characteristic of constituent particles. This present case study deals with the evaluations of the stress–strain behavior of the constituent particles under uniaxial compression of micro-pillars (Singh et al. 2015).

The SEM micrograph (Fig. 4a) shows two types of constituent particles (one black and another white). The corresponding EDS analysis (Fig. 4b) indicates that the bright particle is Fe-bearing inclusions and the dark particle is Si-bearing inclusion. The approximate atomic ratio of Al, Cu, and Fe in Fe-bearing inclusion is 7:2:1, indicating them to be Al_7Cu_2Fe. Similarly, for Si-bearing inclusion, the atomic ratio of Mg and Si is 2:1, indicating them to be Mg_2Si. The micro-pillar fabrication sequence for Mg_2Si using dual-beam focused ion beam (FIB) is shown in Fig. 4c–f. The same procedure was followed for Al_7Cu_2Fe and Al7075 matrix. Initially, a circular trench of ~25 µm diameter was milled out (shown in Fig. 4c), which provides clearance for the flat punch during compression. A course pillar with ~7 µm was made at the inclusion center (refer to Fig. 4d). Further, the pillar diameter was reduced to ~3.5 µm (Fig. 4e), and milling was continued until an aspect ratio of 2.7–3.4 was maintained. During the final process, a low current was utilized, so the taper is less than 3° (shown in Fig. 4f).

The SEM micrographs before loading and after fracture of the pillars are shown in Fig. 5a1, b1, c1 and a2, b2, c2, respectively. The stress–strain behavior of the constituent particles and the matrix of the repeat test is shown in Fig. 5d. Linear stress–strain behavior is observed till fracture for the Al_7Cu_2Fe particles. The fracture stress is ~2.5 ± 0.2 GPa, and strain is approximately 2%. SEM micrograph of the fractured pillar (Fig. 5a2) indicates catastrophic failure. In the case of the Mg_2Si particle, the stress value increased linearly with strain in the initial region, followed by strain bursts. The significant strain hardening is due to the dislocation activity, which is also visible in the SEM micrograph (steps indicated by the arrow in Fig. 5b2). The compressive yield strength of Mg_2Si was calculated to be ~1.8 ± 0.1 GPa. The Al7075 matrix has similar stress–strain behavior as Mg_2Si with a lower yield strength of ~0.5 ± 0.1 GPa. The strength values are in-line with the hardness value obtained by nanoindentation (Kim et al. 2020), i.e., the highest hardness for Al_7Cu_2Fe particle followed by Mg_2Si particle and Al7075 matrix.

Previously, studies have been conducted on the evaluation of mechanical properties of Al_7Cu_2Fe and Mg_2Si by fabricating bulk samples through the powder metallurgy route. While both Al_7Cu_2Fe and Mg_2Si were found to be brittle (Laplanche et al. 2014; Wang et al. 2007; Muñoz-Palos et al. 1996; Takeuchi et al. 1996), limited plasticity for Mg_2Si was observed in this study. This difference in behavior could be attributed to the difference in microstructure like grain size, defect concentration, and type (such as residual porosity), etc. It has been recently shown in several micro-pillar compression studies that a brittle
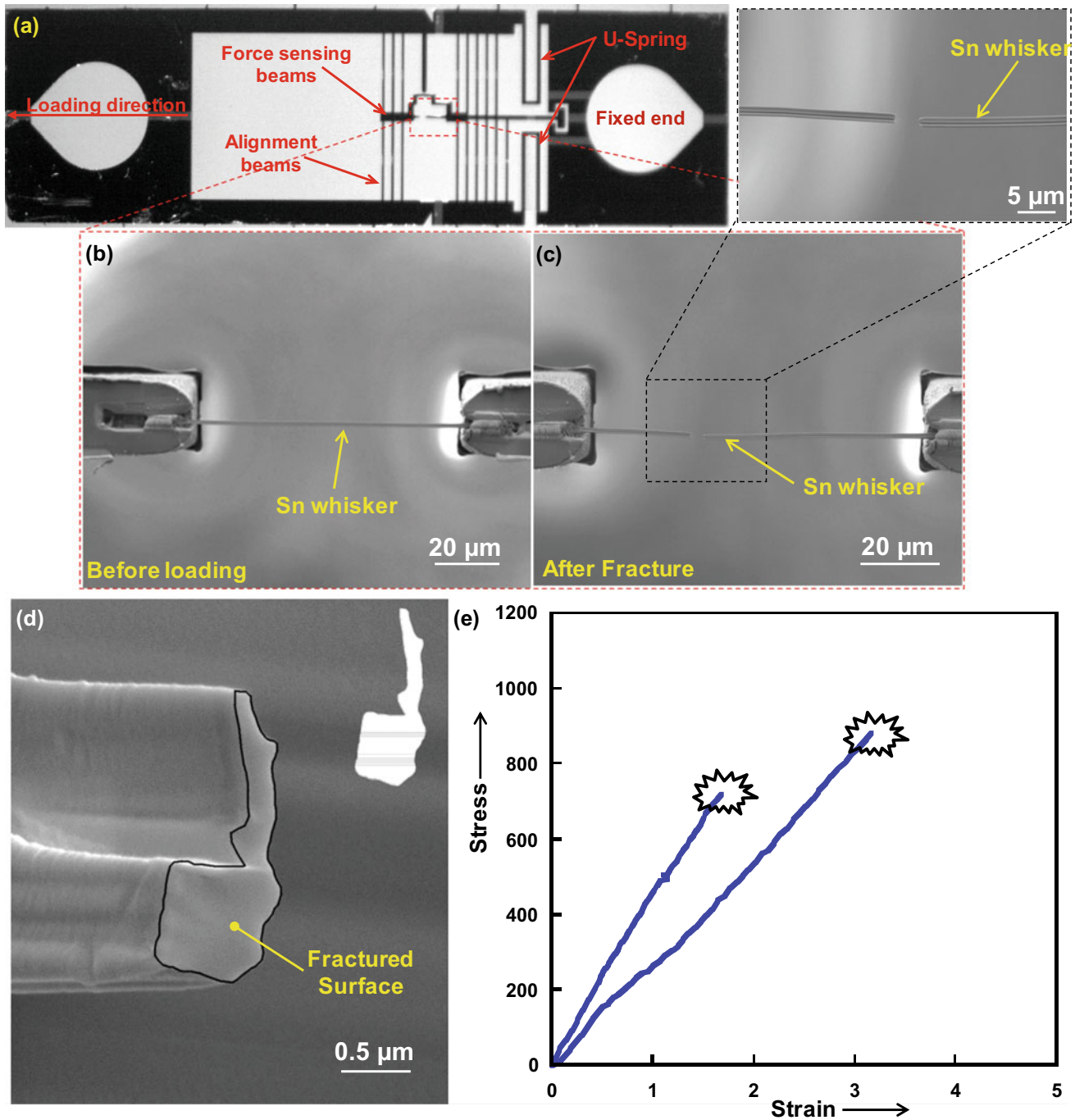
Fig. 3 **a** Optical micrograph of MEMS stage for tensile testing of whisker, **b** zoomed image of Sn whisker before loading, **c** fracture Sn whisker, **d** SE micrograph of fractured surface and inset is a binary image of the fractured surface, **e** nominal stress–strain in the behavior of Sn whisker (Singh et al. 2014a)

material (in bulk) can show plastic deformation at a small length scale (Östlundet 2009; Michler et al. 2007; Korte and Clegg 2011; Östlund 2011). Hence, reducing the size of the sample suppresses cracking, resulting in plastic deformation when the test sample is made significantly small (Östlundet

2009). Oswald (2003) evaluated the hardness and Young's modulus using nanoindentation and predicated stress–strain behavior. Even though the highest strength and modulus was reported for Al$_7$Cu$_2$Fe, a similar yield strength was predicated for Al-matrix and Mg$_2$Si due to their similar hardness
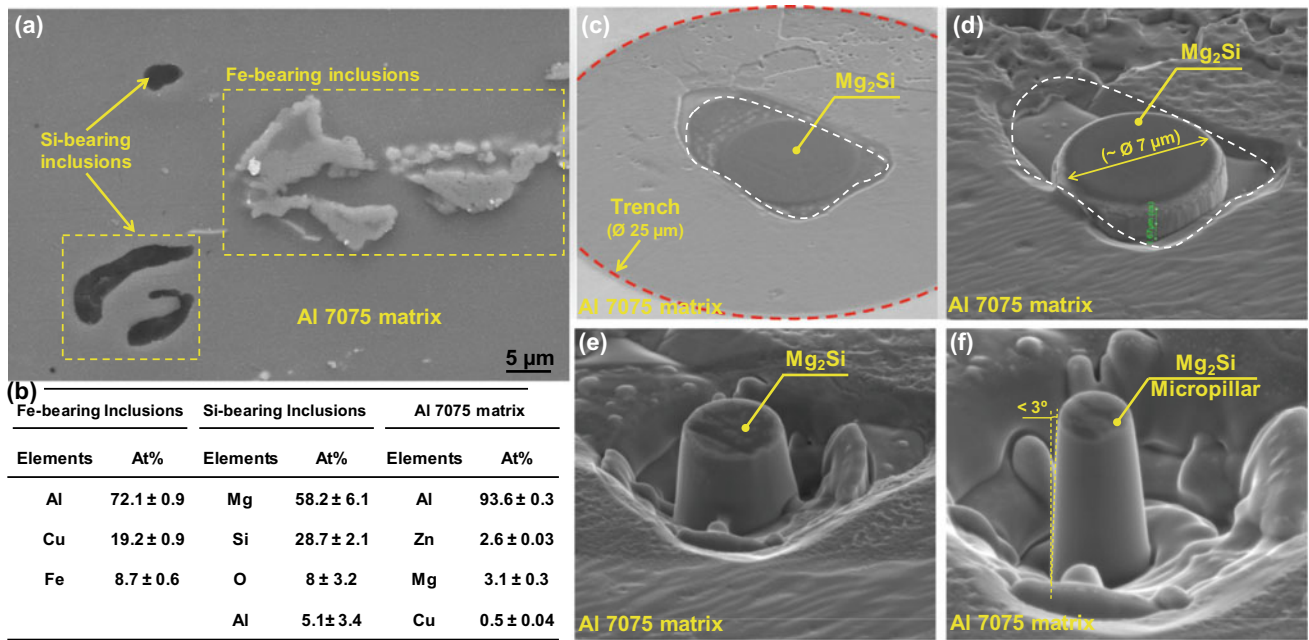
Fig. 4 **a** SEM image showing Fe- and Si-bearing inclusions in Al7075, **b** EDS analysis of the second-phase particles, and **c–f** micro-pillar fabrication using dual-beam FIB
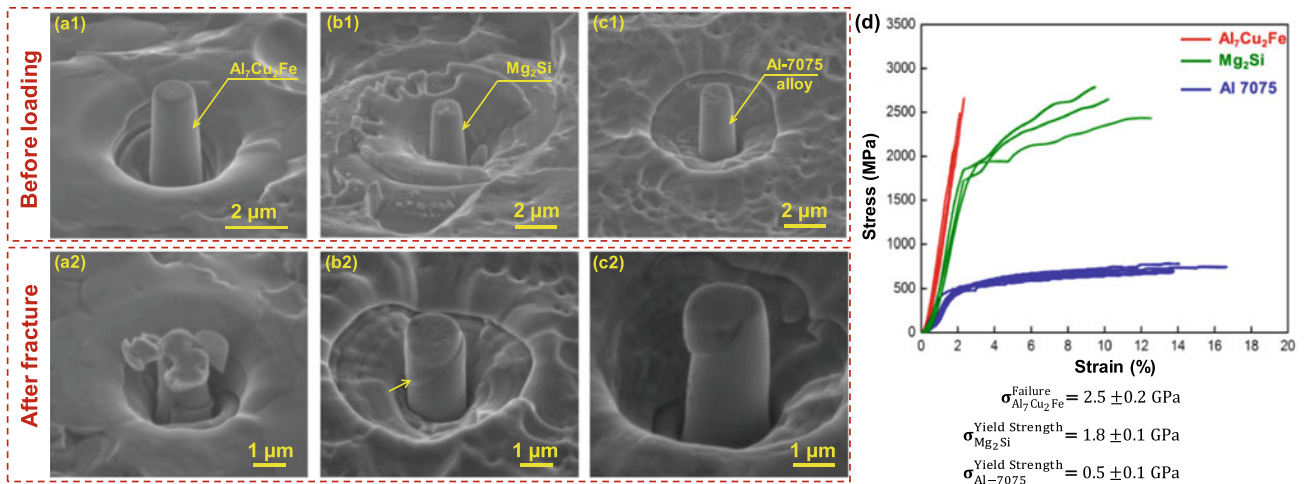
Fig. 5 **a1**, **b1**, **c1** and **a2**, **b2**, **c2** show Al_7Cu_2Fe, Mg_2Si, Al7075 micro-pillars before loading and after fracture, respectively, and **(d)** stress–strain behavior of the second-phase particles and the matrix (Singh et al. 2015)

values. However, the present study shows that Mg_2Si exhibits higher yield strength as compared to the matrix, which corroborates with the hardness values reported in other studies (Singh et al. 2014c).

In summary, the mechanical properties of the constituent particles were evaluated by micro-pillar compression testing, the knowledge of which will allow a better understanding of the bulk deformation behavior of Al7075 alloys.

2.3 Case Study III: Role of Second-Phase Particles on the Deformation Behavior of AZ80 Magnesium Alloys

The role of second-phase particles on the deformation behavior of AZ80 alloy has been divided into two separate studies. One study (Sarvesha et al. 2021) deals with understanding the role of these particles on the fracture process of

the alloy using *in-situ* tensile testing, and another study (Sarvesha et al. 2020) is on the measurement of mechanical properties of the particles using micro-pillar compression.

2.3.1 Effect of Second-Phase Particle on Crack Propagation in Magnesium alloy via *in-situ* Tensile Testing

Magnesium and its alloys exhibit the highest strength-to-weight ratio, which assists in a weight reduction, thus have potential in the automobile, aerospace, and electronics industries (Kulekci 2008; Blawert et al. 2004). Mg-Al-Zn alloys, designated as AZ series alloys, which are a prominent class of magnesium alloys, contain Mg-Al precipitate and Al-Mn inclusions, (Zindal et al. 2018,2017). These second-phase particles have been found to affect the mechanical properties of magnesium alloys significantly (Lugo et al. 2011; Yakubtsov et al. 2008).

A typical as-cast optical micrograph (OM) of Mg-9.3Al-0.45Zn-0.15Mn is shown in Fig. 6a, which shows two types of micron-sized second-phase particles. The corresponding backscattered electron (BSE) image (Fig. 6b) shows gray and white particles due to difference in composition. The energy dispersive spectroscopy (EDS) map (Fig. 6c) shows that the gray particle is enriched with Mg and Al with Zn segregation. In contrast, the white particle is enriched with Mn and Al with the segregation of Fe and Si. Furthermore, the optical microscopic image (dark field mode) shows that Mg-Al precipitate has porosities, which is called a discontinuous eutectic precipitate. In addition, additional dark regions (indicated by arrows in Fig. 6a) correspond to continuous precipitates, which are formed adjacent to eutectic precipitate (refer SE micrograph in Fig. 6b). Electron backscatter diffraction (EBSD) maps suggest that the micron-sized Mg-Al precipitate corresponds to $Mg_{17}Al_{12}$ (space group $I\bar{4}3m$), which are polycrystalline and forms along the grain boundaries of the α-Mg matrix, whereas the Al-Mn inclusion corresponds to Al_8Mn_5 particle (space group $R3m$) and has a rhombohedral crystal structure.

Gatan *in-situ* tensile testing stage, along with the sample dimension, are shown in Fig. 7a, b, respectively. The sequence of secondary electrons (SE) micrographs at different strain (ε) levels (refer Fig. 7c) shows that crack propagation occurred predominantly through $Mg_{17}Al_{12}$ precipitates. The visible crack appeared at strain (ε) 0.0376. To further ascertain the strain at which the crack initiates in $Mg_{17}Al_{12}$, in-situ testing was performed with a focus on a single $Mg_{17}Al_{12}$ particle, as shown in Fig. 8a. It can be observed that at $\varepsilon = 0.017$, the crack initiates in the second-phase particle, which is in the linear portion of the stress–strain curve (shown in inset). With an increase in strain, more cracks appear perpendicular to the loading direction, as indicated by arrows in Fig. 8a.

Further, to understand the strain partitioning between the matrix and the precipitate, *in-situ* tensile testing, assisted with EBSD, was performed. A 70° pre-tilt in-situ stage (shown in Fig. 7a) was employed for EBSD scanning. The secondary electron (SE) micrographs (at 70° tilt) along with the EBSD maps, before loading and after fracture, are shown in Fig. 8b, c, respectively. Kernel average misorientation (KAM) maps in Fig. 8b, c are generated from EBSD scanning. KAM calculates the average misorientation between each pixel and its nearest neighbors and indicates strain in different phases during external loading. KAM map in Fig. 8b shows no strain in the matrix as well as in the particle before loading. However, after fracture, the strain is predominately distributed in the matrix, as the matrix shows higher KAM values (Fig. 8c). The KAM value of the precipitate is approximately zero, indicating the $Mg_{17}Al_{12}$ fractured in a brittle manner.

Previously, Yakubtsov et al. (2008) observed an increase in the ductility of AZ80 (Mg-8.2Al-0.51Zn) alloy with a decrease in the volume fraction of $Mg_{17}Al_{12}$ precipitate. Lü et al. (2000) observed the crack formation near $Mg_{17}Al_{12}$ precipitate during tensile deformation, and it was postulated that the crack initiated at the interface between $Mg/Mg_{17}Al_{12}$. In the present study, it is evident from *in-situ* tensile testing, fracture initiates at $Mg_{17}Al_{12}$ at low strain and propagates through the $Mg_{17}Al_{12}$ phase.

2.3.2 Mechanical Property Evaluation of Second-Phase Particle in Magnesium Alloy by Micro-pillar Compression

It is clear from the previous study (Sect. 2.3.1) that the second-phase particles significantly affect the deformation characteristics of magnesium alloys. Therefore, it is essential to understand the mechanical properties of the individual particle. However, due to the small size of these particles, their mechanical properties cannot be evaluated by conventional techniques. Thus, this study deals with the evaluation of mechanical properties (stress–strain behavior) of these second-phase particles using *in-situ* micro-pillar compression (Sarvesha et al. 2020).

The micro-pillar fabrication process has already been discussed in Case II. The undeformed and deformed pillars of the matrix and second-phase particles are shown in Fig. 9, and the stress–strain behavior is shown in Fig. 10a. During compression, slip bands form on the α-Mg matrix surface (shown in Fig. 8a1 inset), which manifests as strain bursts in stress–strain curves (Fig. 10a)—a general characteristic of ductile metals/alloy (Schneider et al. 2013). In contrast, the stress–strain behavior of $Mg_{17}Al_{12}$ showed linear behavior until a massive strain burst (Fig. 10a). The corresponding SE micrograph shows a noticeable change in the shape of the $Mg_{17}Al_{12}$ pillar (Fig. 9b2), which could be due to strong
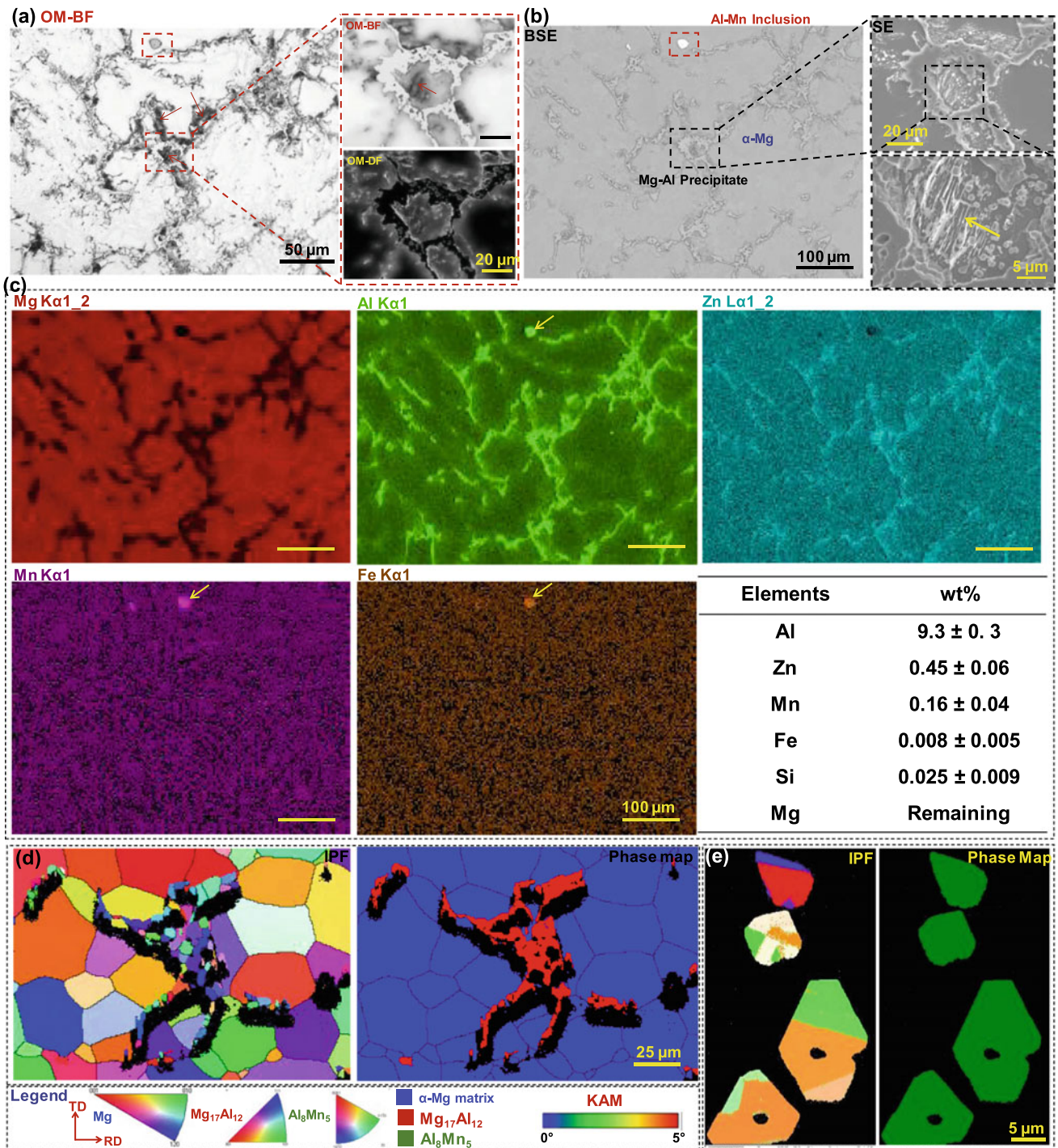
Fig. 6 **a** Optical micrograph (OM)-bright filed (BF) image, **b** SE micrograph, **c** EDS map of Mg, Al, Zn, Mn and Fe. **d**, **e** EBSD maps of $Mg_{17}Al_{12}/\alpha$-Mg matrix and Al_8Mn_5 particle, respectively

strain localization without dislocation movement (Song et al. 2018). Further, it is evident from the stress–strain behavior of Al_8Mn_5 (Fig. 10a) particle that it exhibits the highest strength and ductility. SEM micrograph of the deformed Al_8Mn_5 pillar (Fig. 9c2) shows slip lines, which manifest as load drops in stress–strain curves (Fig. 10a). Al_8Mn_5 particle

exhibits the highest yield strength of $\sim 3084 \pm 630$ MPa, followed by $Mg_{17}Al_{12}$ with $\sim 814 \pm 141$ MPa, and α-Mg matrix with $\sim 134 \pm 22$ MPa.

The site-specific transmission electron microscopy (TEM) of Al_8Mn_5 deformed micro-pillar shows the dislocation structure (shown by the arrow in Fig. 10b). It can be
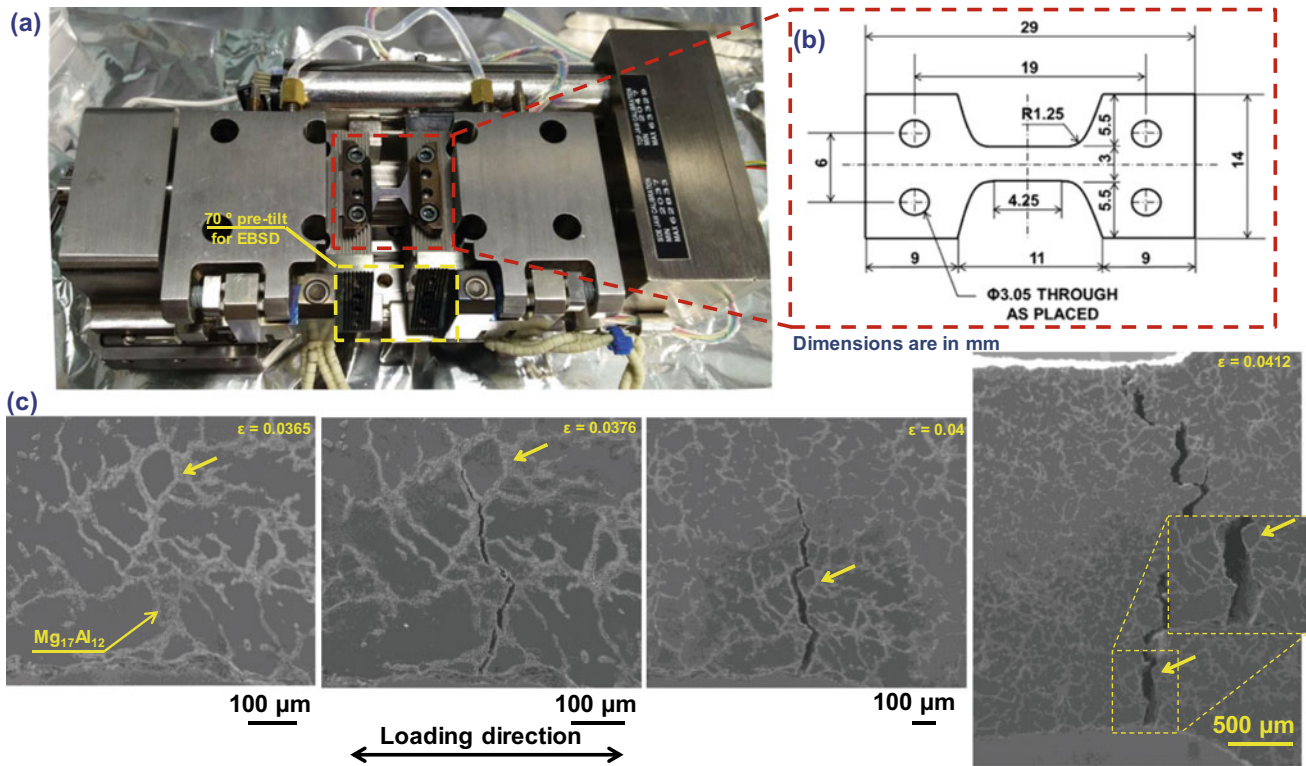
Fig. 7 **a** In-situ tensile testing stage, **b** sample dimension, **c** SEM images showing crack propagation through $Mg_{17}Al_{12}$ precipitates (arrow indicate reference region) in an as-cast sample

noticed that one type of dislocation structure is queued on the slip plane. The selective area diffraction pattern (SADP) along the $[100]$ zone axis is shown in Fig. 10c. The angle between $(01\bar{1})$ and (021) is around 88.7°, which corresponds to the rhombohedral crystal structure (Zeng et al. 2018).

Additionally, to verify the deformation behavior of each phase, qualitative analysis was also performed using nanoindentation. The indentation was performed at 60 mN load for the Al_8Mn_5 particle and 35 mN load for the $Mg_{17}Al_{12}$ particle and the matrix. SEM micrographs, atomic force microscopy (AFM) images, and corresponding line profiles of the indents made on the Al_8Mn_5 particle, the $Mg_{17}Al_{12}$ particle, and the matrix are shown in Fig. 10d–f, respectively. The line profiles along the corner (*C*) to edge (*E*) were used to observe the pile-up and sink-in phenomenon. Line profiles for the Al_8Mn_5 particle clearly show pile-up along all the edges, whereas the $Mg_{17}Al_{12}$ particle does not show pile-up or sink-in along the edges. The α-Mg matrix shows both pile-up and sink-in (indicated in AFM in Fig. 10f). In addition, both pile-up and sink-in were visible along the same edge of the indent (shown in SE micrograph in Fig. 10f). It is already known that the plastically deformable materials show pile-up characteristics (Fischer-Cripps 2004). The observed pile-up's in the case of Al_8Mn_5 particle corroborate with the observation made

previously, i.e., the Al_8Mn_5 particles exhibit ductility. In contrast, the absence of pile-up and sink-in in the case of $Mg_{17}Al_{12}$ particles indicates the absence of plastic deformation, which is also evident from micro-pillar compression (Fig. 9).

A couple of studies are available for the bulk deformation of $Mg_{17}Al_{12}$ (Ragani et al. 2011; Fukuchi and Watanabe 1980). However, no study has been carried out to evaluate the stress–strain behavior of Al_8Mn_5 particles. Ragani et al. (2011) fabricated bulk $Mg_{17}Al_{12}$ through levitation casting and measured the room temperature compressive fracture strength and strain to be ~ 325 MPa and $\sim 2\%$, respectively. Fukuchi and Watanabe (1980) evaluated the bulk properties of $Mg_{17}Al_{12}$ at elevated temperature (between 360 and 435 °C), where particles were found to exhibit ductility. However, it should be noted that both the studies were carried out in the bulk form, which can show different properties than that at a small length scale. In fact, it has been shown that the mechanical response at large and small length scales might be different (Singh et al. 2015; Michler et al. 2007; Korte and Clegg 2011). In the present case, interestingly, the $Mg_{17}Al_{12}$ particle exhibits distinct behavior at room temperature, i.e., sudden failure after a significant strain burst, unlike the brittle nature reported in the bulk samples (Ragani et al. 2011).
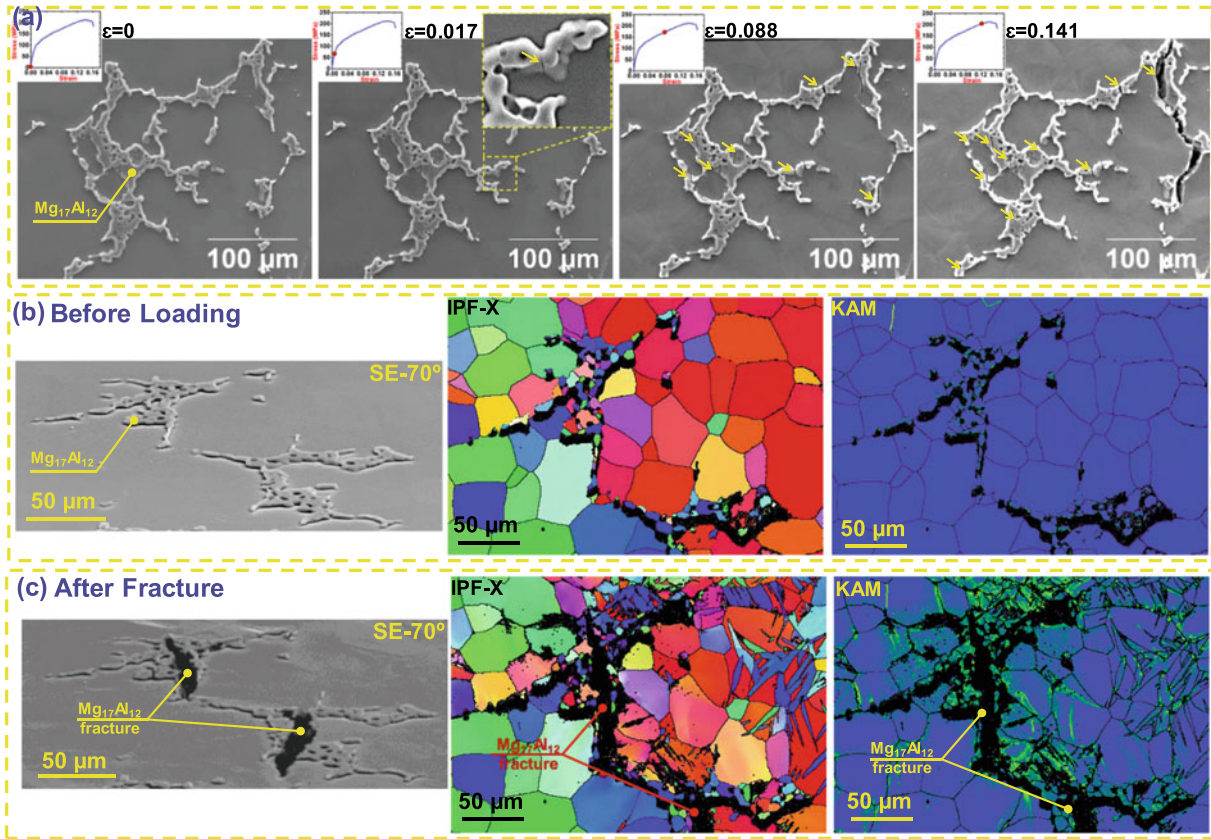
Fig. 8 **a** SEM micrographs of in-situ tensile testing of $Mg_{17}Al_{12}$ at different strain levels along with the stress–strain diagram. SE micrograph and corresponding area IPF-X and KAM map **b** before loading and **c** after fracture. (Loading is along *X* direction). (For legends, refer Fig. 6)
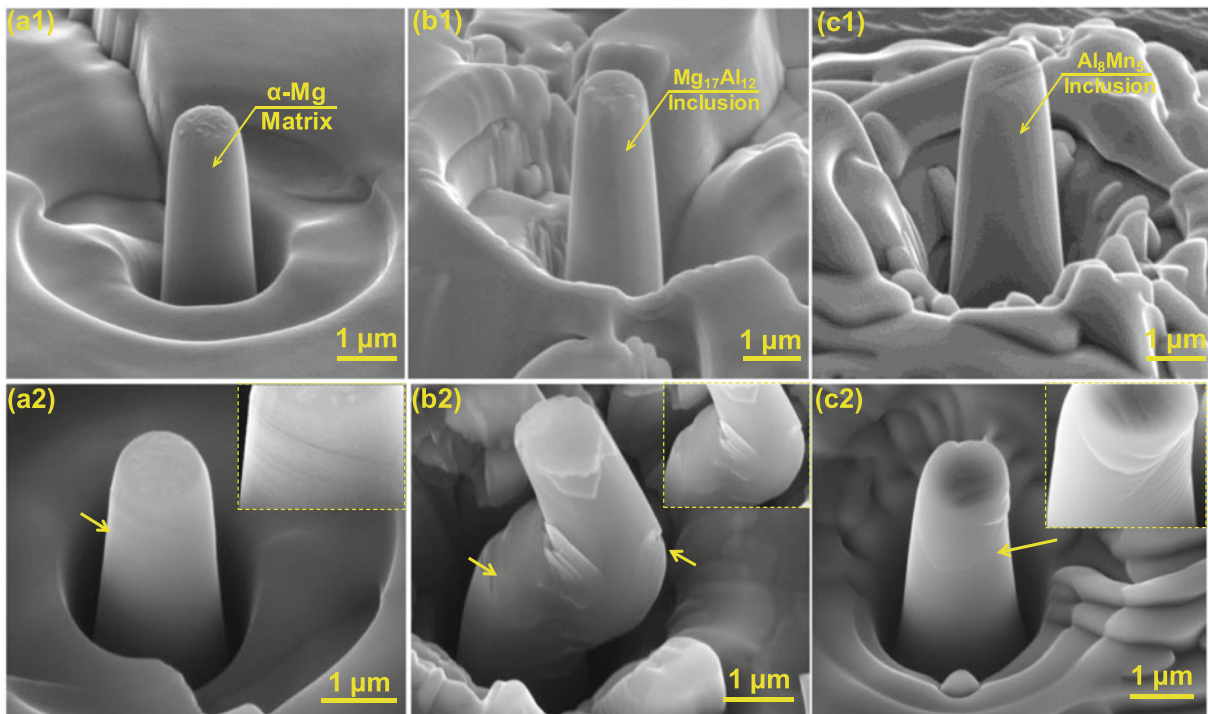
Fig. 9 **a1**, **b1**, **c1** and **a2**, **b2**, **c2** before and after deformation of α-Mg matrix, $Mg_{17}Al_{12}$, and Al_8Mn_5 micro-pillar, respectively (Sarvesha et al. 2020)
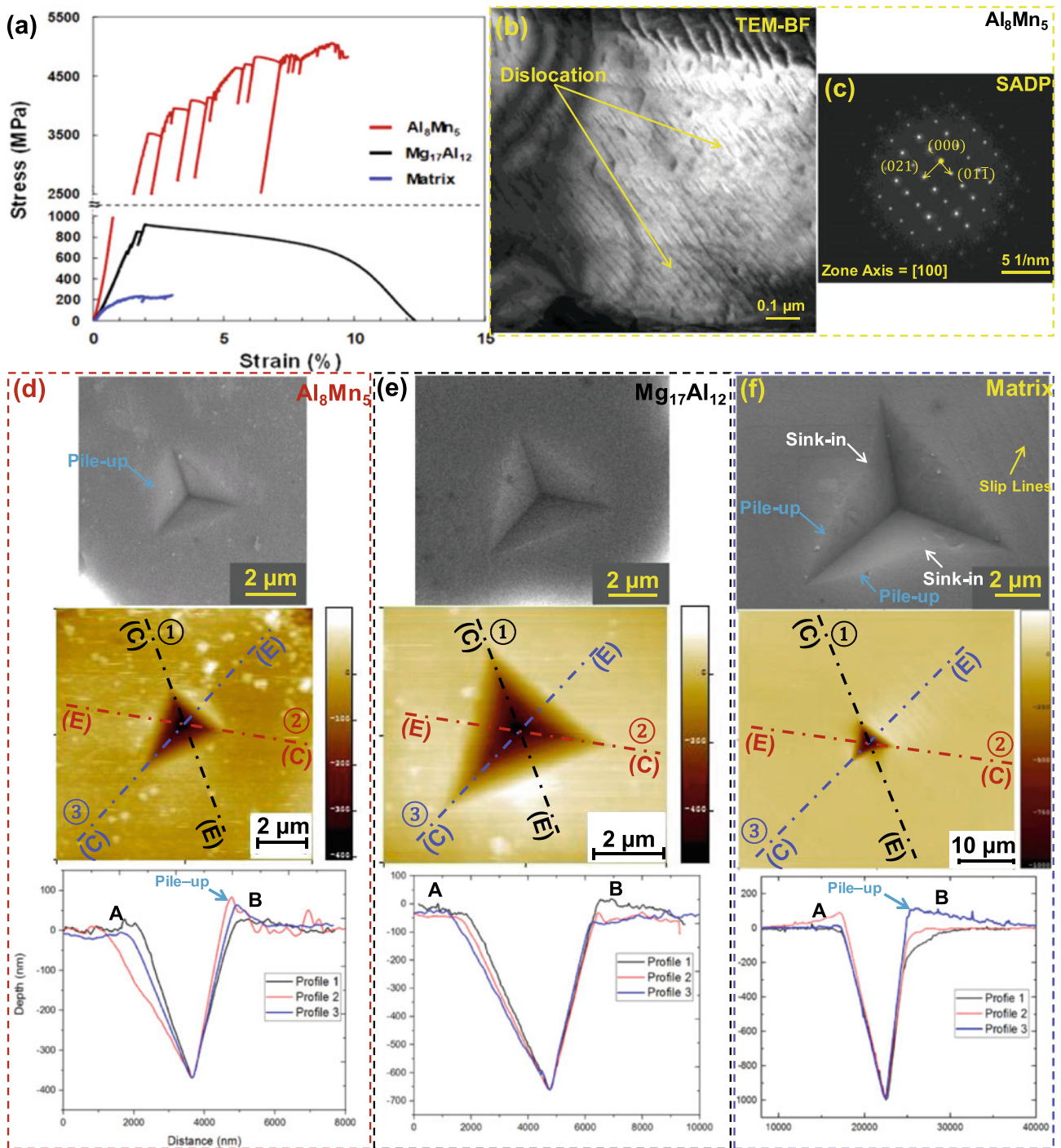
Fig. 10 a Stress–strain behavior of the matrix and particles, **b** TEM-BF, and **c** SADP of deformed Al_8Mn_5 pillar. **d–f** are the SE micrographs, AFM images, and line profile of the indents made using nanoindentation on Al_8Mn_5, $Mg_{17}Al_{12}$, and α-Mg matrix, respectively (Sarvesha et al. 2020)

3 Summary

The mechanical properties of materials change significantly with a reduction in size. Due to the inherent problems associated the conventional mechanical testing in understanding the deformation behavior of materials at a small length scale, *in-situ* electron microscopy has gained interest in recent years. The advancement in instrumentation in the electron microscopes, such as FIB and nanoindentation in SEM, has made it possible to understand the deformation behavior in real time. Also, techniques such as EBSD/ECCI/DIC assist in the quantification of the deformation characteristics of the materials. The present article shows the importance of electron microscopy in understanding the deformation behavior of metallic systems by using three case studies.

References

Fischer-Cripps AC (2004) Nanoindentation, 2nd ed. Springer, New York

Armstrong DEJ, Hardie CD, Gibson JSKL, Bushby AJ, Edmondson PD, Roberts SG (2015) Small-scale characterisation of irradiated nuclear materials: part II nanoindentation and micro-cantilever testing of ion irradiated nuclear materials. J Nucl Mater 462:374–381

Blawert C, Hort N, Kainer KU (2004) Automotive applications of magnesium and its alloys. Trans Indian Inst Metals 57(4):12

Bucci RJ, Warren CJ, Starke EA Jr (2000) Need for new materials in aging aircraft structures. J Aircr 37(1):122–129

Dimiduk DM, Uchic MD, Parthasarathy TA (2005) Size-affected single-slip behavior of pure nickel microcrystals. Acta Mater 53(15):4065–4077

Dunn BD (1987) Eur Space Agency (ESA) J 11:1

Fukuchi M, Watanabe K (1980) Tensile behavior of γ-phase in Al-Mg system at elevated temperatures. J Japan Inst Light Metals 30(5):253–257

Galyon GT (2005) Annotated tin whisker bibliography and anthology. IEEE Trans Electron Pack Manuf 28(1):94–122

Gianolaet DS (2011) In situ nanomechanical testing in focused ion beam and scanning electron microscopes. Rev Sci Instrum 82(6):063901

Guo E-Y, Singh SS, Xie H, Williams JJ, Jing T, Chawla N (2014) Microstructure-based modeling of deformation in steels based on constitutive relationships from micropillar compression. Steel Res Int 85(6):946–953

Han JH, Saif MTA (2006) In-situ microtensile stage for electromechanical characterization of nanoscale freestanding films. Rev Sci Instrum 77(4):045102

Han JH, Rajagopalan J, Saif MTA (2007) MEMS-based testing stage to study electrical and mechanical properties of nanocrystalline metal films. In: MEMS/MOEMS components and their applications IV, vol 6464, p 64640C

Kim J, Plancher E, Tasan CC (2020) Hydrogenation-induced lattice expansion and its effects on hydrogen diffusion and damage in Ti–6Al–4V. Acta Mater 188:686–696

Korte S, Clegg WJ (2011) Discussion of the dependence of the effect of size on the yield stress in hard materials studied by microcompression of MgO. Phil Mag 91(7–9):1150–1162

Kulekci MK (2008) Magnesium and its alloys applications in automotive industry. Int J Adv Manuf Technol 39(9–10):851–865

Laplanche G, Bonneville J, Joulain A, Gauthier-Brunet V, Dubois S (2014) Mechanical properties of Al-Cu-Fe quasi crystalline and crystalline phases: an analogy. Intermetallics 50:54–58

Legros M, Gianola DS, Motz C (2010) Quantitative in-situ mechanical testing in electron microscopes. MRS Bull 35:354–360

Lü YZ, Wang QD, Ding WJ, Zeng XQ, Zhu YP (2000) Fracture behavior of AZ91 magnesium alloy. Mater Lett 44(5):265–268

Lugo M, Jordon JB, Horstemeyer MF, Tschopp MA, Harris J, Gokhale AM (2011) Quantification of damage evolution in a 7075 aluminum alloy using an acoustic emission technique. Mater Sci Eng A 528(22–23):6708–6714

Maire E, Zhou S, Adrien J, Dimichiel M (2011) Damage quantification in aluminium alloys using in situ tensile tests in X-ray tomography. Eng Fract Mech 78(15):2679–2690

Mathew S, Osterman M, Pecht M, Dunlevey F (2009) Evaluation of pure tin plated copper alloy substrates for tin whiskers. Circuit World 35(1):3–8

Michler J, Wasmer K, Meier S, Östlund F, Leifer K (2007) Plastic deformation of gallium arsenide micropillars under uniaxial compression at room temperature. Appl Phys Lett 90(4):043123

Muñoz-Palos JM, del Cristina MC, Adeva P (1996) Synthesis of Mg_2Si powder by mechanical alloying and its consolidation. Mater Trans Japan Inst Metals Mater 37(10):1602–1606

Östlund F (2011) Ductile-brittle transition in micropillar compression of GaAs at room temperature. Phil Mag 91(7–9):1190–1199

Östlundet F (2009) Brittle-to-ductile transition in uniaxial compression of silicon pillars at room temperature. Adv Func Mater 19(15):2439–2444

Oswald LE (2003) Effects of microstructure on high-cycle fatigue of an Al-Zn-Mg-Cu Alloy (Al-7055). Masters thesis, School of Engineering, University of Pittsburgh, Pittsburgh, PA

Payne J, Welsh G, Christ RJ Jr, Nardiello J, Papazian JM (2010) Observations of fatigue crack initiation in 7075–T651. Int J Fatigue 32(2):247–255

Pearson S (1975) Initiation of fatigue cracks in commercial aluminium alloys and the subsequent propagation of very short cracks. Eng Fract Mech 7(2):235–240

Powell BE, Skove MJ (2004) Elastic strength of tin whiskers in tensile tests. J Appl Phys 36(4):1495

Proff C, Abolhassani S, Dadras MM, Lemaignan C (2010) In-situ oxidation of zirconium binary alloys by environmental SEM and analysis by AFM, FIB, and TEM. J Nucl Mater 404(2):97–108

Ragani J, Donnadieu P, Tassin C, Blandin JJ (2011) High-temperature deformation of the γ-$Mg_{17}Al_{12}$ complex metallic alloy. Scripta Mater 65(3):253–256

Sarvesha R, Ghori U-R, Chiu YL, Jones IP, Singh SS, Jain J (2020) Mechanical property evaluation of second phase particles in a Mg-8Al-0.5Zn alloy using micropillar compression. Mater Sci Eng A 775:138973

Sarvesha R, Chalapathi D, Yadava M, Singh SS (2021) *In-situ* studies on deformation and fracture characteristics of AZ91 Mg alloy. Materialia 18:101177. https://doi.org/10.1016/j.mtla.2021.101177

Schneider AS, Kiener D, Yakacki CM, Maier HJ, Gruber PA, Tamura N, Kunz M, Minor AM, Frick CP (2013) Influence of bulk pre-straining on the size effect in nickel compression pillars. Mater Sci Eng A 559:147–158

Singh SS, Sarkar R, Xie H-X, Mayer Rajagopalan CJ, Chawla N (2014) Tensile behavior of single-crystal tin whiskers. J Electron Mater 43 (4):978–982

Singh SS, Williams JJ, Hruby P, Xiao X, De Carlo F, Chawla N (2014) In-situ experimental techniques to study the mechanical behavior of materials using X-ray synchrotron tomography. Integr Mater Manuf Innov 3(1):109–122

Singh SS, Schwartzstein C, Williams JJ, Xiao X, De Carlo F, Chawla N (2014c) 3D microstructural characterization and mechanical properties of constituent particles in Al 7075 alloys using X-ray synchrotron tomography and nanoindentation. J Alloy Compd 602:163–174

Singh SS, Guo E, Xie H, Chawla N (2015) Mechanical properties of intermetallic inclusions in Al 7075 alloys by micropillar compression. Intermetallics 62:69–75

Singh SS, Williams JJ, Stannard TJ, Xiao X, Carlo FD, Chawla N (2016) Measurement of localized corrosion rates at inclusion particles in AA7075 by In-Situ three-dimensional (3D) X-ray synchrotron tomography. Corros Sci 104:330–335

Singh SS, Stannard TJ, Xiao X, Chawla N (2017) In Situ X-ray microtomography of stress corrosion cracking and corrosion fatigue in aluminum alloys. JOM 69(8):1404–1414

Slama MBH, Maloufi N, Guyon J, Bahi S, Weiss L, Guitton A (2019) In-Situ macroscopic tensile testing in SEM and electron channeling contrast imaging: pencil glide evidenced in a bulk β-Ti₂1S polycrystal. Material 12(15):2479

Song G, Kong T, Dusoe KJ, Canfield PC, Lee S-W (2018) Shear localization and size-dependent strength of YCd₆ quasicrystal approximant at the micrometer length scale. J Mater Sci 53 (9):6980–6990

Starke EA, Staley JT (2011) 24—application of modern aluminium alloys to aircraft. In: Lumley R (ed) Fundamentals of aluminium metallurgy. Woodhead Publishing, pp 747–783

Takeuchi S, Hashimoto T, Suzuki K (1996) Plastic deformation of Mg₂Si with the C1 structure. Intermetallics 4(Suppl. 1):S147–S150

Uchic MD, Dimiduk DM, Florando JN, Nix WD (2004) Sample dimensions influence strength and crystal plasticity. Science 305 (5686):986–989

Volkert CA, Donohue A, Spaepen F (2008) Effect of sample size on deformation in amorphous metals. J Appl Phys 103:083539

Wang L, Qin XY, Xiong W, Zhu XG (2007) Fabrication and mechanical properties of bulk nanocrystalline intermetallic Mg₂Si. Mater Sci Eng A 459(1–2):216–222

Weiland H, Nardiello J, Zaefferer S, Cheong S, Papazian J, Raabe D (2009) Microstructural aspects of crack nucleation during cyclic loading of AA7075-T651. Eng Fract Mech 76(5):709–714

Wisner B, Cabal M, Vanniamparambil PA, Hochhalter J, Leser WP, Kontsos A (2015) In-situ microscopic investigation to validate acoustic emission monitoring. Exp Mech 55(9):1705–1715

Xue Y, El Kadiri H, Horstemeyer MF, Jordon JB, Weiland H (2007) Micromechanisms of multistage fatigue crack growth in a high-strength aluminum alloy. Acta Mater 55(6):1975–1984

Yakubtsov IA, Diak BJ, Sager CA, Bhattacharya B, MacDonald WD, Niewczas M (2008) Effects of heat treatment on microstructure and tensile deformation of Mg AZ80 alloy at room temperature. Mater Sci Eng A 496(1–2):247–255

Zeng G, Xian JW, Gourlay CM (2018) Nucleation and growth crystallography of Al₈Mn₅ on B₂-Al(Mn, Fe) in AZ91 magnesium alloys. Acta Mater 153:364–376

Zindal A, Jain J, Prasad R, Singh SS, Cizek P (2017) Correlation of grain boundary precipitate characteristics with fracture and fracture toughness in an Mg-8Al-0.5 Zn alloy. Mater Sci Eng A 706:192–200

Zindal A, Jain J, Prasad R, Singh SS, Sarvesha R, Cizek P, Barnett MR (2018) Effect of heat treatment variables on the formation of precipitate free zones (PFZs) in Mg-8Al-0.5Zn alloy. Mater Charact 136:175–182